https://doi.org/10.5194/egusphere-2026-3277
Preprint. Discussion started: 29 June 2026

The role of temperature and salinity on ocean alkalinity enhancement performance

Matías Saez Moreno[1], Jens Hartmann[1], Janine Börker[1], Peggy Bartsch[1] and Charly A. Moras[1]

[1]Department of Earth System Sciences, University of Hamburg, Hamburg, Germany

Correspondence to: Matías Sáez M. (matias.saez@uni-hamburg.de)

Abstract. Ocean alkalinity enhancement (OAE) is a promising carbon dioxide removal approach but its effectiveness is constrained by uncertainties in dissolution kinetics and carbonate precipitation under varying ocean conditions. Here, we systematically quantified the dissolution and net alkalinity delivery of three common OAE feedstocks, i.e., $NaHCO_3$, $Ca(OH)_2$, $Mg(OH)_2$, across 16 temperature–salinity combinations ($T = 4, 12, 20, 28$°C and $S = 24, 29, 34, 38$). Each treatment targeted an alkalinity increase of 500 μmol kg^{-1} and was monitored over 11 days to track changes in total alkalinity (TA) and dissolved inorganic carbon (DIC). Results showed that $NaHCO_3$ dissolved rapidly and nearly completely under all conditions, reliably delivering the intended alkalinity. $Ca(OH)_2$ delivered high net alkalinity in cold waters, but its effectiveness declined with increasing temperature and salinity. Net TA losses occurred at 28°C and $S \geq 29$, likely driven by secondary $CaCO_3$ precipitation and particle passivation. $Mg(OH)_2$ dissolved more slowly and exhibited strong salinity dependence: near–complete dissolution occurred at $S \leq 34$ and lower temperatures, while higher salinity ($S = 38$) significantly inhibited dissolution, causing net TA losses at higher temperatures. The observed dissolution kinetics, including likely effects of secondary $CaCO_3$ precipitation, were well described by a modified Noyes–Whitney function. A first application suggests that $NaHCO_3$ is the most predictable feedstock across tested global conditions; $Ca(OH)_2$ has more potential in cold environments but loses efficiency when temperature increases; and $Mg(OH)_2$ is kinetically slower and susceptible to high–salinity inhibition. Experiment and global extrapolation imply that the carbon dioxide removal potential and efficiency are highly dependent on the combination of feedstock and environmental control.

1 Introduction

Climate change is one of humanity's most urgent challenges. According to the Intergovernmental Panel on Climate Change, exceeding 1.5°C above preindustrial levels could trigger serious impacts, such as more frequent and intense droughts, heatwaves, and heavy rainfalls (IPCC, 2023). While the reduction of carbon dioxide (CO_2) emissions remains the primary strategy, current trajectories suggest that climate stabilization will also require carbon dioxide removal (CDR) methods (Friedlingstein et al., 2025). One CDR approach that is receiving more attention is ocean alkalinity enhancement (OAE) (Gagern et al., 2022; Oschlies et al., 2023). OAE aims at increasing seawater total alkalinity (TA), which lowers surface partial pressure of carbon dioxide (pCO_2) and promotes passive air–sea CO_2 uptake. This CO_2 is then retained in the ocean as dissolved inorganic carbon (DIC) over long timescales (Kheshgi, 1995; Renforth and Henderson, 2017). Common candidate feedstocks include sodium bicarbonate ($NaHCO_3$), calcium hydroxide ($Ca(OH)_2$) and magnesium hydroxide ($Mg(OH)_2$), due to their technical viability. These materials differ strongly in dissolution behavior and precipitation risk, offering unique advantages and trade-offs (Eisaman et al., 2023; Hartmann et al., 2023; Moras et al., 2022, 2024; Varliero et al., 2024a, b). Despite the potential of OAE, many studies have identified carbonate precipitation as one of the main risks, especially when particles act as nucleation surfaces that facilitate mineral growth (Hartmann et al., 2023; Marion et al., 2009; Moras et al., 2022; Suitner et al., 2024). If high aragonite saturation levels (Ω_{Ar}) are reached, a runaway precipitation process may even be triggered, leading to a net loss of alkalinity and potential CO_2 leakage. However, the environmental conditions that control this risk are still not well defined.

Furthermore, a persistent uncertainty in OAE is how environmental variables like salinity and temperature influence the mineral dissolution kinetics and the resulting stability of the added TA. Both will also dictate the effectiveness of atmospheric CO_2 sequestration of OAE (Renforth & Henderson, 2017). Although existing laboratory and mesocosm studies provide valuable insights, most focus on specific conditions (typically ~25°C, salinity ~35) or examine one of these variables in isolation (e.g. Hartmann et al., 2023; Moras et al., 2024; Varliero et al., 2024a, b; Yang et al., 2023). As a result, the combined effects are not completely understood. An additional key limitation in current OAE assessments is that most large-scale ocean models assume complete and instant dissolution of added alkaline materials (e.g. Ilyina et al., 2013; Wang et al., 2023). This simplification neglects the strong dependence of TA generation on dissolution kinetics and carbonate chemistry, which can lead to an overestimation of the carbon–uptake potential, especially when dissolution is incomplete or delayed. To achieve more realistic model predictions, it is essential to develop empirically derived dissolution functions that explicitly depend on environmental conditions.

To address these gaps, we conducted a systematic experiment testing the dissolution of $NaHCO_3$, $Ca(OH)_2$, and $Mg(OH)_2$ across 16 combinations of temperature (4, 12, 20, 28°C) and salinity (24, 29, 34, 38) to replicate an extensive range of ocean conditions. From these data, we derived empirical, model–ready parameterizations of the effective net TA gain as functions of temperature, salinity, and time, explicitly incorporating dissolution, CO_2 ingassing, and early–stage precipitation effects. The primary aims of this study are: (1) to understand how temperature, salinity and, mineral type influence dissolution kinetics and the resulting alkalinity release, and (2) to develop empirical functions that reliably predict net TA gain based on temperature and salinity for each material, thus improving assessment accuracy of OAE's effectiveness.

2 Material and Methods

2.1 Laboratory Experiments

2.1.1 Experimental Setup

Four temperature levels were chosen (4, 12, 20, and 28°C) to represent a broad latitudinal gradient from polar to tropical surface ocean conditions. These temperatures were controlled and maintained using a walk-in climate chamber (Weiss

Technik UK). Salinity was adjusted to four representative levels (24, 29, 34, 38), spanning brackish coastal waters to highly saline basins. As a starting point, we used natural seawater collected in the North Sea (54.93° N, 6.43° E; initial salinity ≈ 34), which was sterile–filtered through a 0.2 µm Whatman Polycap 75 AS filter. Lower salinities were obtained by dilution with MilliQ-purified water (18.2 MΩ), and the highest salinity was produced by controlled passive evaporation inside the climate chamber at 25°C to avoid abrupt changes. These adjustments were controlled using a Multiline IDS 3320, resulting in four independent seawater batches.

We established four experimental runs: each corresponding to one of the four temperature conditions and all the selected seawaters, resulting in 48 experimental bottles (three materials × four temperatures × four salinities). Each material–temperature–salinity combination was performed as a single independent experimental unit, similar to a time–series design, where multiple samples were collected over time from the same bottle to observe the evolution of dissolution and alkalinity (Iglesias-Rodríguez et al., 2023). This approach focused on capturing the process dynamics across the environmental gradient rather than estimating variability among multiple replicates per treatment. Because of this, no bottle-level replication was included, and each treatment was represented by a single bottle.

To avoid contamination, the bottles (1 liter LDPE) were cleaned sequentially by overnight soak in a 1 % NaOH solution, three rinses with tap water, overnight soak in a 0.5% HCl, and three rinses with tap water followed by three rinses with MilliQ. The bottles were then dried at 50°C overnight. Prior to each run, seawater batches were equilibrated with water-saturated ambient air in the climate chamber for 48–72 h to achieve a stable chemical equilibrium with the ambient air's partial pressure of CO_2 at the specific target temperatures as per Moras et al., 2023.

In each run, the bottles were filled with ~1 kg seawater and dosed with the respective material (reagent-grade, Carl Roth Brand) to achieve a net alkalinity addition (ΔTA_{target}) of 500 µmol kg^{-1}. This corresponded to 42 mg kg^{-1} for $NaHCO_3$, 18.5 mg kg^{-1} for $Ca(OH)_2$, and 14.6 mg kg^{-1} for $Mg(OH)_2$. This target value was selected to allow direct comparison with previous studies and for being considered a safe upper limit for pH increase in ecosystems (Hartmann et al., 2023; Moras et al., 2022, 2026; Santinelli et al., 2024; Suitner et al., 2024; Varliero et al., 2024a, b). All materials were dried at 50°C overnight and weighed with a Kern ABT 120-5DNM balance (± 0.01 mg, < 1 % uncertainty). Grain size distribution was conducted on a Bettersizer S3 Plus and revealed different D50 between $NaHCO_3$ and the two other minerals, with a D50 of 80.99 µm for $NaHCO_3$ and D50 values of 31.98 and 29.79 µm for $Ca(OH)_2$ and $Mg(OH)_2$, respectively.

Bottles were mixed continuously on an orbital shaker (26-mm stroke) at 100 revolutions per minute (RPM), preventing long-term particle settling. Bottles remained capped during the experiment, but were opened during measurement and sampling, creating intermittent air exposure. Headspace volume increased progressively due to sample removal, ultimately limiting the experiment to 11 days. Initial carbonate chemistry varied with temperature and salinity: TA = 1646–2616 µmol kg^{-1}, DIC = 1562–2456 µmol kg^{-1}, pH on the total scale (pH_T) = 7.77–8.20, and Ω_{Ar} = 0.87–3.19. Exact initial values are provided in the Supplementary Dataset and served as baselines for carbonate-system calculations.

2.1.2 Sampling and Measurement

Sampling was conducted at 0, 2, 8, 12, 24, 32, 48, 72, 96, and 264 h using a peristaltic pump connected to a 0.2 µm filter (Sartorius) and a 14-gauge needle to withdraw water from the bottom of each bottle. Approximately 75 g of sample was removed per event: ~35 g for TA, ~25 g for DIC, plus overflow for DIC samples of ~15 g. Samples were stored in cold, dark conditions following Dickson et al. (2007).

To check the experiment's progress, temperature, salinity, and pH were controlled in situ using a Multiline IDS 3320 with a TetraCon 925 conductivity cell (calibrated using 0.01 mol L^{-1} KCl) and a SenTix 940 pH electrode (calibrated with NIST-traceable WTW buffers, pH 4.006, 6.865, 9.180). The control measurements were done every hour during the first 12 h, every 2 h between 24 and 32 h, every 4 h between 48 and 56 h, and at 72, 80, 96, and 264 h (Table 1).

Table 1. Mean measured temperature and salinity and their respective standard deviations for all experimental treatment combination during the experiment. Values are reported to demonstrate the stability of the controlled conditions.

Temperature Target (°C)	Measured Temperature (°C)	Salinity Target	Measured Salinity
4	4,044 ± 0,062	**24**	24,294 ± 0,076
12	11,64 ± 0,133	**29**	29,177 ± 0,152
20	19,757 ± 0,110	**34**	34,152 ± 0,223
28	27,883 ± 0,097	**38**	38,167 ± 0,619

TA was measured via open cell titration in technical duplicates using a Metrohm Titrando with 0.02 mol kg^{-1} HCl. DIC was measured in technical quintuplicates using a Shimadzu TOC–L analyzer, maintaining the average of the three best measurements as the final value. Certified Reference Materials (Batch #207, Dickson Laboratory) were used to calibrate the instruments before and after each measurement session, and were analyzed alongside the samples to calculate correction factors (Dickson, 2021). Using the measured TA and DIC values, carbonate chemistry variables (e.g., pH_T, Ω_{Ar}) were computed using pyCO2SYS (Humphreys et al., 2022) with Lueker et al. (2000) constants for K1 and K2, Dickson (1990) for $KHSO_4$, and Dickson and Riley (1979) for KHF. The additional Ca^{2+} from $Ca(OH)_2$ dissolution was accounted for in all calculations. Saturation indices (SIs) were computed in PHREEQC (Pitzer database; Parkhurst and Appelo, 2013) using seawater ionic compositions from Millero et al. (2008).

2.2 Parameterization Setup

2.2.1 Fitted Function

Given that most observed ΔTA trajectories were dissolution–dominated and showed monotonic increases over time, we parameterized the system using a modified Noyes–Whitney formulation. This function describes the observed pattern of rapid early dissolution followed by an asymptotic approach to a plateau (Goldsmith et al., 1978; Noyes and Whitney, 1897).

Treatments exhibiting net alkalinity loss were excluded from the fitting procedure, because exponential rise functions cannot represent declining trajectories.

Net alkalinity (ΔTA) was used to capture the combined effects of mineral dissolution and likely secondary precipitation. ΔTA was normalized to the 500 µmol kg^{-1} target to define the dimensionless alkalinity fraction f_A, dependent on salinity (S), temperature (T) and time (t), and defined as:

$$f_{\mathrm{A}}(S,T,t) \; = \; \frac{\Delta\mathrm{TA}_{\mathrm{measured}}(S,T,t)}{\Delta\mathrm{TA}_{\mathrm{target}}} \tag{1}$$

This variable ranges from 0 (no net TA gain) to 1 (full realization of the target increase).

The evolution of Eq. (1) was parameterized using a modified Noyes–Whitney equation with a saturation parameter, which accounts for deviations from ideal first–order kinetics (Dokoumetzidis et al., 2006; Weibull, 1951). The function is expressed as:

$$f_{\mathrm{A}}(S,T,t) \; = \; a(S,T)\left[1-\exp\left((-k(S,T)\;t)^{\beta(S,T)}\right)\right] \tag{2}$$

where a is the asymptotic fraction, k is the apparent rate constant and β is the saturation–related curvature parameter.

As β can vary, Eq. (2) generalizes the classical Noyes–Whitney model, providing a compact empirical description of how much and how fast the net alkalinity release proceeds under a given environmental condition.

Fitting was performed using SciPy curve_fit with bounded parameters. For each material, 16 independent fits (4 S × 4 T) yielded the corresponding 16 estimates of a, k, and β. Model skill was evaluated using adjusted R^2, RMSE, and inspection of residual patterns. The Akaike Information Criterion (AIC) was used to decide whether relaxing β improved model performance (Akaike, 1987).

2.2.2 Derivation of Temperature–Salinity Functions

To generalize the fitted parameters from our environmental conditions, we used an Ordinary Least Squares (OLS) regression to express a, k, and β as empirical functions of S and T. OLS was selected as it is reproducible and avoids overfitting given the small sample size. Predictor terms included linear, polynomial, and inverse functions of S and T. Candidate predictor combinations were tested based on statistical performance (adjusted R^2 and RMSE), visual agreement with the fitted time series, and residual behavior. Potential outliers were only excluded if they were clearly inconsistent with the overall experimental pattern and could be justified mechanistically.

3 Results

3.1 Experimental Results

Across the full temperature–salinity matrix, $NaHCO_3$ nearly reached the ΔTA_{target} across all experimental conditions, whereas the hydroxides showed strong environmental dependencies. $Ca(OH)_2$ showed lower ΔTA gains with rising temperature and salinity, eventually leading to TA loss at 28°C for $S \geq 29$. $Mg(OH)_2$ exhibited reliably ΔTA gains at low to moderate salinities, but it was strongly inhibited at $S = 38$, with net alkalinity loss at 20 and 28°C (Figs. 1 and A1).

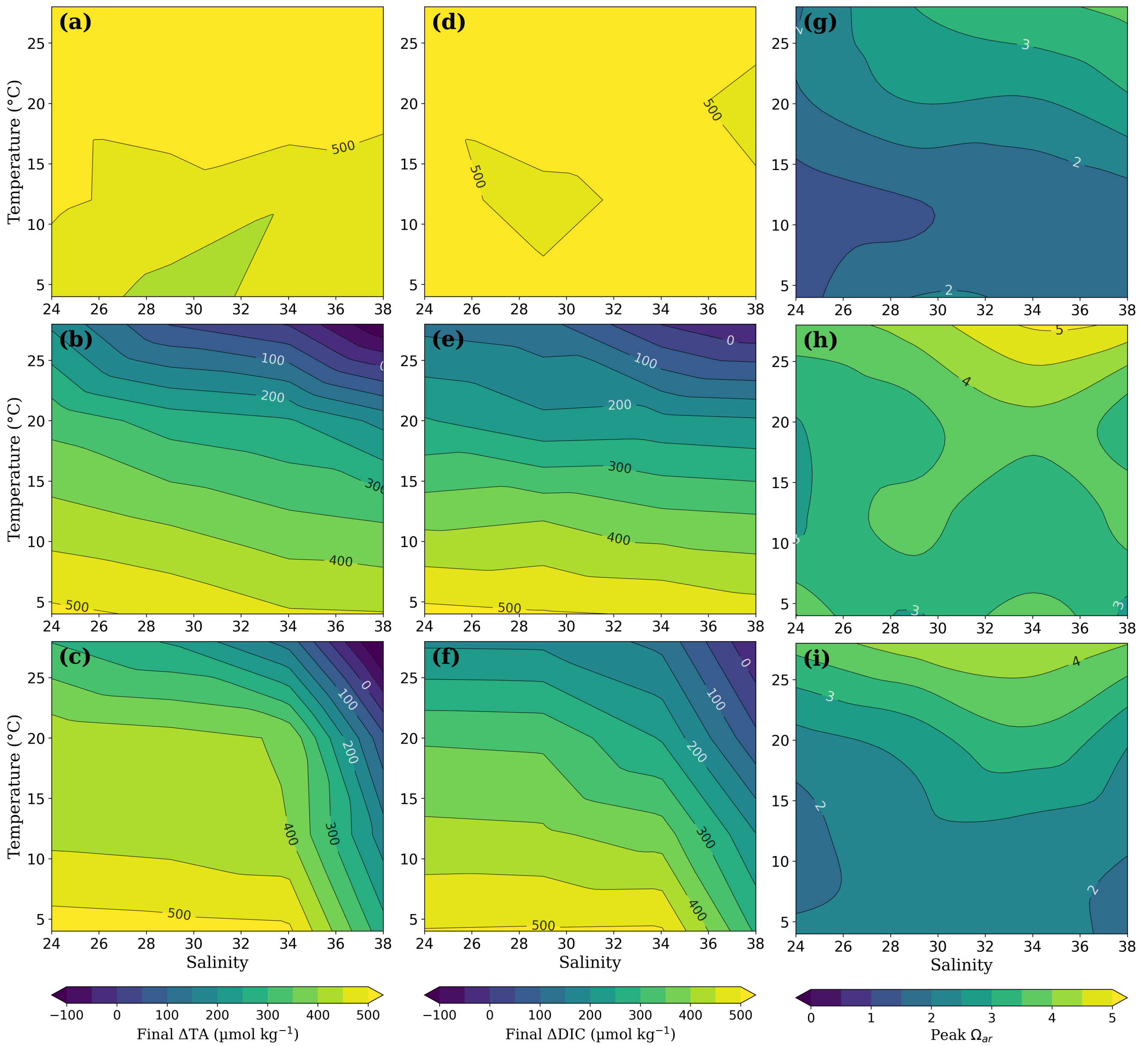

Figure 1: Contour plots of the carbonate system response after 11 days across the experimental temperature (4–28 °C) and salinity (24–38) gradients for three alkalinity materials. In each row, (a, d, g) represent $NaHCO_3$, (b, e, h) $Ca(OH)_2$, and (c, f, i) $Mg(OH)_2$. Panels (a–c), (d–f), and (g–i) show final ΔTA, final ΔDIC, and the maximum Ω_{Ar} reached during the experiment, respectively, relative to initial conditions.

3.1.1 $NaHCO_3$

For $NaHCO_3$, ΔTA virtually achieved the 500 µmol kg^{-1} target addition under all T–S combinations (Figs. 1a and A1a). At 4 and 12°C, final ΔTA varied slightly with salinity but remained high throughout the experiment (mean 475 ± 34 µmol kg^{-1}).

At 20 and 28°C, ΔTA became more uniform across salinities (mean 517 ± 15 µmol kg^{-1}), achieving full dissolution. On average, considering all the treatments, ΔTA reached 474 ± 31 µmol kg^{-1} after 2 h and 493 ± 30 µmol kg^{-1} by day 11.

ΔDIC increased rapidly during the first hours for all the cases (mean 483 ± 40 µmol kg^{-1}) and stabilized near 500 µmol kg^{-1}, reaching an average of 516 ± 20 µmol kg^{-1} at 264 h (Figs. 1d and A2a). Ω_{Ar} showed small transient peaks but minimal net change, with slightly higher values at increased temperature and salinity (Figs. 1g and A3a). Overall, $NaHCO_3$ dissolution was complete and showed no evidence of alkalinity loss under any tested conditions.

3.1.2 $Ca(OH)_2$

$Ca(OH)_2$ showed strong dependence on temperature and secondary sensitivity to salinity (Fig. 1b). ΔTA rose rapidly during the first 24–48 h followed by either stabilization or a subsequent decline, depending on conditions (Fig. A1b). At 4°C, ΔTA increase was efficient, reaching ~90% of the expected change within 48 h, and final ΔTA values were 478 ± 28 µmol kg^{-1} on average across all salinities. At 12°C, ~75% of the total increase occurred within 48 h, but ΔTA gain slowed abruptly afterwards, plateauing at markedly lower values (mean 378 ± 33 µmol kg^{-1}). This pattern persisted at 20°C, where ΔTA levelled off at progressively lower plateaus with increasing salinity (~330 µmol kg^{-1} at S=24 to ~200 µmol kg^{-1} at S=38). At 28°C, the increase only occurred during the initial 12 h, and except for S = 24, all salinities showed clear declines, including net alkalinity loss at S = 38.

ΔDIC trajectories generally mirrored ΔTA trends but with larger variability and at slower pace, especially at high temperatures and salinities (Fig. 1e). At 4°C, ΔDIC approached ~500 µmol kg^{-1}, but increasing temperature made the values stabilize at much lower levels, becoming negatives at 28°C (Fig. A2b). Ω_{Ar} showed early peaks of ~3–4 within the first 24–48 h followed by a return toward initial levels, except under conditions where ΔTA declined at 28°C, where Ω_{Ar} showed two pronounced peaks ~5 and remained >4 for extended periods (Figs. 1h and A3b).

3.1.3 $Mg(OH)_2$

$Mg(OH)_2$ displayed strong salinity dependence and slower kinetics than $Ca(OH)_2$, showing two distinct trends: (i) higher ΔTA values at salinities 24–34, and (ii) strong inhibition at S = 38 (Figs. 1c and A1c). At 4°C, the three lower salinity incubations approached ΔTA_{target} (mean 517 ± 6 µmol kg^{-1}), but with a more gradual alkalinity release, requiring four days to reach ~90% of the expected change. At 12 and 20°C, salinities 24, 29 and 34 showed similar dynamics with slower but continued increases, yielding ~400 µmol kg^{-1} at the end of the experiment. At 28 °C, salinity altered the patterns, with S = 24 and 29 continuingly rising (final ΔTA ~300 and ~250 µmol kg^{-1}), whereas S = 34 plateaued at ~130 µmol kg^{-1}.

The second group, S=38, showed an inhibited response across all temperatures, reaching its highest value of ~300 µmol kg^{-1} at 4°C. With increasing temperature, final ΔTA values declined progressively, reaching 174 µmol kg^{-1} at 12°C and 64 µmol kg^{-1} at 20°C. At 28°C, the initial 24 hours showed a weak increase but then declined sharply, resulting in net alkalinity loss of -174 µmol kg^{-1}.

ΔDIC followed the same overall trends as ΔTA, with larger fluctuations at high T-S combinations and overall slower response (Figs. 1f and A2c). Ω_{Ar} exhibited moderate peaks of ~2–3 from 4 to 20°C, and stronger and more sustained peaks of ~3–4 at 28°C (Figs. 1i and A3c). By day 11, Ω_{Ar} ranged between 1.2 and 3.2 across treatments.

3.2 Model Fitting and Parameterization

The ΔTA time−series data were fitted with the modified Noyes−Whitney equation introduced in the Material and Methods section, yielding the corresponding functions for the alkalinity-increment fraction f_A. The derived parameters *a, k* and β for each material, together with their statistical performance, are summarized in Table 2. Their resulting temperature–salinity dependencies are visualized in Fig. 2 as contour surfaces.

Table 2. Empirical functions for $NaHCO_3$, $Ca(OH)_2$, and $Mg(OH)_2$ with their respective parameters (asymptotic fraction *a*, apparent rate constant *k*, and saturation curvature β). For some cases, the parameter is represented by an empirical function of S and T; for others, a fixed value is used. Statistical metrics are also reported.

	$f_A^{NaHCO_3}$	$f_A^{Ca(OH)_2}$	$f_A^{Mg(OH)_2}$
$a(S,T)$	$0.8786 + 0.136\,TS^{-1}$	$1.4121 - 0.0264\,T - 0.0118\,S$	$-2.8039 - 0.0053\,S^2 + 0.2915\,S - 0.0004\,TS$
$k(S,T)$	19.05	$0.9972 + 0.0029\,T^2 - 2.5964\,T^{-1} - 0.0951\,T + 0.0008\,S$	$0.0463 - 0.0014\,T - 0.0032\,ST^{-1}$
$\beta(S,T)$	1.0	1.0	$0.2269 + 2.4303\,T^{-1} + 3.3525\,S^{-1}$
Adjusted R²	0.965	0.934	0.894
RMSE	0.05	0.05	0.06

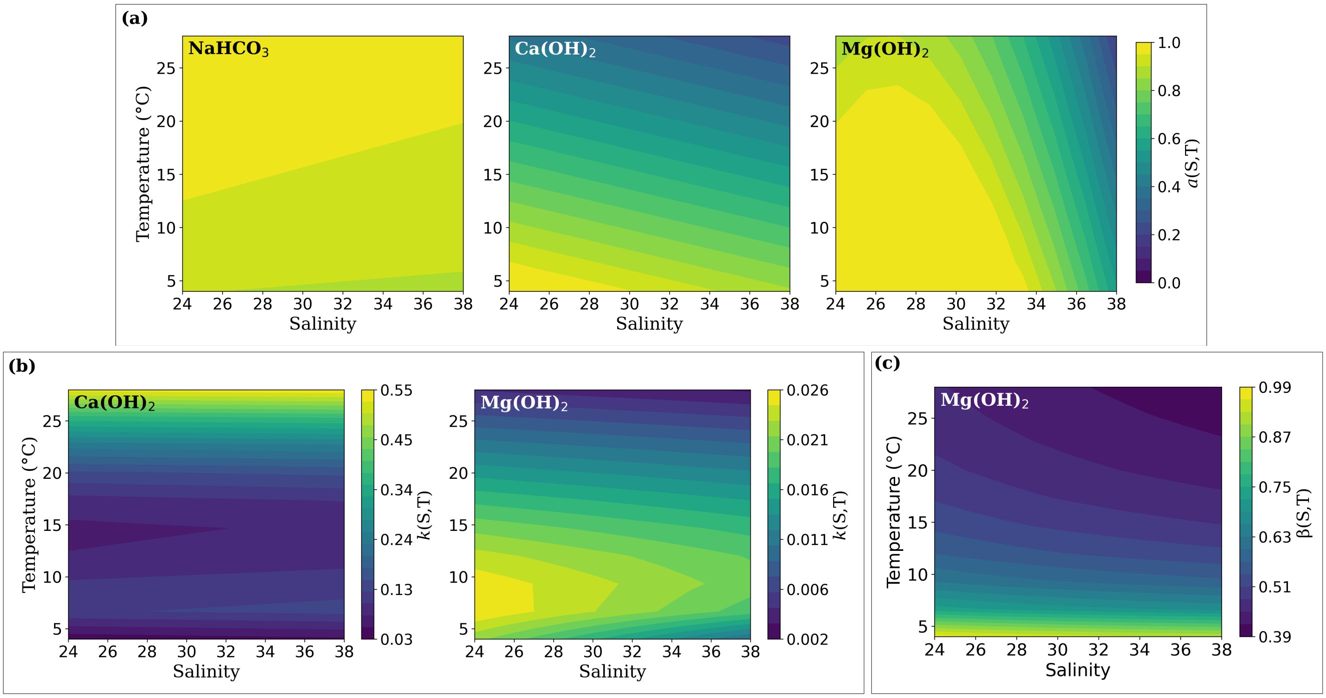

Figure 2. Contour surfaces of the empirical parameters (a) asymptotic fraction *a*, (b) apparent rate constant *k*, and (c) saturation curvature β as functions of salinity and temperature for the tested materials (see Table 1). Parameters that remain constant and show no T–S dependence are not included.

Figure 3 provides an example comparison of the observed data and the modelled f_A at 12 °C across the salinity range; the corresponding fits for the other temperatures are provided in the Appendix in Fig. A4.

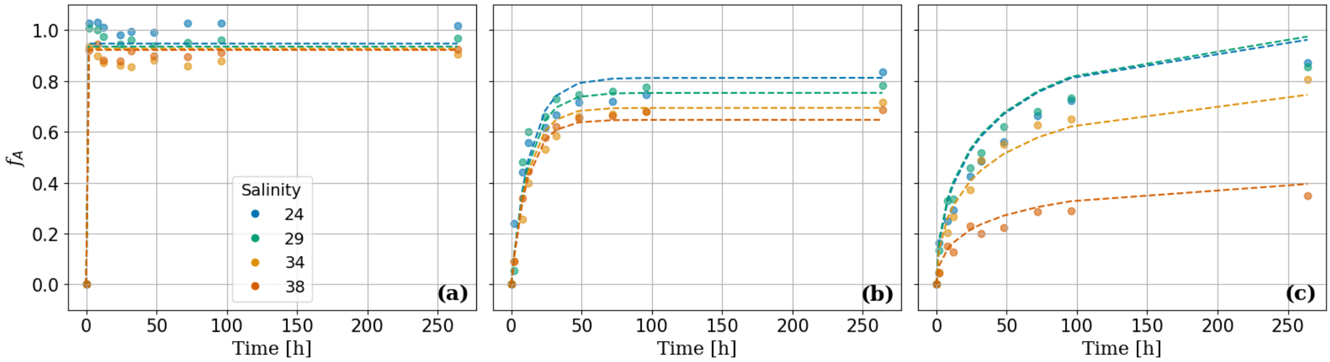

Figure 3. Observed and modelled alkalinity–increment fraction (f_A) over time at 12 °C for (a) NaHCO$_3$, (b) Ca(OH)$_2$, and (c) Mg(OH)$_2$ across the experimental salinity range (24–38). Data points denote measured values and dashed lines show predictions using the fitted parameterization (Eq. 2). Full time–series fits for all temperatures are provided in the Appendix (Fig. A4).

3.2.1 $NaHCO_3$ Parameterization

The asymptotic dissolved fraction (*a*) for $NaHCO_3$ ranged from 0.91 to 0.99 over all treatments. Final values were slightly lower at 4 and 12°C, while 20 and 28°C produced uniformly high *a* values close to 1 (Fig. 2a). Rate constant *k* was consistently large (19.05 ± 0.07 h^{-1}) and showed no meaningful dependence on temperature or salinity, which favored a model with a constant value under all scenarios. As the AIC did not reveal significant improvement with a free β, the parameter was fixed to 1. Overall, for all T–S conditions, the empirical model achieved an average adjusted R^2 of 0.965 and RMSE of 0.05 (Fig. A4a; Tables B3 and B4).

3.2.2 $Ca(OH)_2$ Parameterization

Fitted values of *a* ranged from 0.24 to 1.00. Values decreased systematically with increasing temperature and exhibited suppression at higher salinity (Fig. 2a). Values of *k* fluctuated between 0.02 and 0.55, declining as temperature and salinity increased (Fig. 2b). Although β estimates ranged from 0.51 to 1.00, AIC comparisons and model stability tests indicated that using $\beta = 1$ did not reduce model quality but rather improved consistency across conditions. Considering all the scenarios, this parameterization achieved an average adjusted R^2 of 0.934 and RMSE of 0.05 (Fig. A4b; Tables B3 and B4).

3.2.3 $Mg(OH)_2$ Parameterization

The parameter *a* decreased from 1.00 at low and moderate salinities to approximately 0.15 at salinity 38 (Fig. 2a). Temperature only had a slight influence on *a* except at the highest salinity. Compared to $Ca(OH)_2$, *k* values were much smaller (0.001–0.025 h^{-1}) and primarily temperature-dependent, with limited salinity influence (Fig. 2b). β varied from 0.35 to 1.00 and declined with increasing temperature (Fig. 2c). Excluding the low performances of $S=38$ at 20 and 28°C from the final evaluation metrics, the empirical function achieved a strong fit, with average adjusted R^2 of 0.894 and RMSE of 0.06 for the whole T–S range (Fig. A4c; Tables B3 and B4).

4 Discussion

4.1 Overall performance of all three alkaline materials of interest

4.1.1 $NaHCO_3$: stable behavior across all conditions

$NaHCO_3$ behaved uniformly across all treatments, dissolving fast and reaching the target, consistent with its high solubility (Rumble, 2021; Table B1). ΔTA and ΔDIC trends progressed nearly in parallel with ΔTA:ΔDIC ratios close to 1:1, and Ω_{Ar} showed minimal fluctuations, suggesting negligible risk of carbonate formation (Figs. 1, A1a, A2a and A3a). This pattern agrees with previous OAE studies using bicarbonate, where alkalinity remains stable, dissolution is not kinetically limited, and precipitation is not thermodynamically favored (Hartmann et al., 2023; Suitner et al., 2024; Varliero et al., 2024a). The negligible influence of temperature and salinity implies that solid–phase constraints did not play a controlling role, i.e. the added alkalinity was immediately present in solution. These findings support $NaHCO_3$ as a highly predictable feedstock, especially in settings where rapid alkalinity delivery is required.

4.1.2 $Ca(OH)_2$: temperature and salinity control alkalinity release and subsequent $CaCO_3$ precipitation

In the case of $Ca(OH)_2$, temperature was the primary driver of the reaction, controlling both dissolution and carbonate formation. Salinity had a secondary role and became more influential under warmer conditions (Figs. 1, A1b and A2b). Although $Ca(OH)_2$ has retrograde solubility, SIs showed that at equilibrium, the material remained undersaturated at all T–S conditions, so its dissolution was thermodynamically possible (Rumble, 2021; Table B1). This indicates that the incomplete alkalinity delivery cannot be attributed to bulk saturation or intrinsic solubility limits, as seen by Varliero et al. (2024b). Additionally, after material addition, SIs for aragonite and calcite increased marginally, suggesting that added Ca^{2+} did not cause a substantial equilibrium shift (Mucci, 1983; Table B2).

Consequently, the main process reducing alkalinity can be attributed to secondary precipitation. It is likely that in the boundary layer, the particle reached higher pH and carbonate concentrations than in the bulk water, creating local supersaturation that could enable heterogeneous nucleation and explain the different patterns, from complete dissolution to net alkalinity loss (Marion et al., 2009; Moras et al., 2022, 2026).

In colder seawater, the conditions are most favorable for $Ca(OH)_2$ dissolution (Varliero et al., 2024b). The added OH^- raises pH and shifts the carbonate system toward higher carbonate proportions, lowering seawater pCO_2 and strengthening the air–sea CO_2 gradient, which is much more efficient at low temperatures (Rohling, 2023; Teng et al., 1996; Weiss, 1974; Zeebe and Wolf–Gladrow, 2001). These processes, combined with constant mixing and slower kinetics for carbonate nucleation, may prevent extreme and sustained Ω_{Ar} peaks, limiting boundary-layer supersaturation and reducing the chance of $CaCO_3$ formation. Thus, the material delivered the expected alkalinity (Figs. 1, A1 and A2).

However, as temperature and salinity rise, seawater's capacity to hold dissolved CO_2 decreases and ingassing becomes less effective. This weakens the buffering capacity and leads to higher, more prolonged Ω_{Ar} peaks (Figs. 1 and A3b). The onset of these peaks coincides with the initiation of the ΔTA plateaus, suggesting that carbonate precipitation begins while dissolution is still ongoing. This behavior is consistent with the concept of a critical alkalinity period, during which alkalinity can be delivered before carbonate supersaturation triggers precipitation that suppresses further dissolution (Moras et al., 2026).

Hence, it is likely that near $Ca(OH)_2$ particles, Ω_{Ar} values are much higher than in the bulk solution, driving the boundary layer into high supersaturation before all the material has dissolved. In addition, higher salinity further elevates Ca^{2+} and CO_3^{2-} activities and raises initial bulk Ω_{Ar}. This promotes heterogeneous precipitation on particle surfaces, potentially in a runaway manner under the most extreme conditions (Marion et al., 2009; Moras et al., 2022; Suitner et al., 2024).

A possible secondary mechanism is passivation. Newly formed $CaCO_3$ may coat dissolving alkaline grains, as observed in pure aqueous systems (Ruiz–Agudo et al., 2013). As suggested by Moras et al. (2026), $CaCO_3$ needles may not simply halt dissolution. Instead, they can provide a long–term substrate and additional surface area for further $CaCO_3$ precipitation, reducing the reactive surface area of $Ca(OH)_2$, promoting net alkalinity loss.

Moreover, Moras et al. (2022, 2026) and Hashim et al. (2025) reported that, during $Ca(OH)_2$ dissolution, once runaway precipitation is initiated, Ω_{Ar} declines from its peak and stabilizes at ~2 as the system approaches a new quasi-equilibrium. Our results show that this stabilization is not exclusive to fully developed runaway events. Even under conditions where alkalinity delivery was only partially suppressed, Ω_{Ar} similarly converged toward values near ~2, suggesting that this value may reflect a more general buffering state, occurring whenever $CaCO_3$ formation becomes sufficiently strong to oppose dissolution, regardless of the extent of precipitation (Fig. A3).

Therefore, the overall $Ca(OH)_2$ performance can be explained by two competing processes: alkalinity addition via dissolution and alkalinity loss through precipitation. Their relative strength depends on temperature, salinity, and CO_2 availability. At low T–S, more CO_2 and limited supersaturation support continuous dissolution, resulting in larger net ΔTA gains. Under intermediate T–S conditions, dissolution remains dominant but is increasingly counterbalanced by localized precipitation, leading to the observed plateau trends. At high T–S, the system crosses a threshold: the boundary layer becomes even more supersaturated and for longer periods. Enhanced nucleation and reduced CO_2 buffering increase the likelihood of runaway precipitation. In this regime, dissolution is strongly limited by secondary $CaCO_3$ formation, severely diminishing or fully negating the effectiveness of $Ca(OH)_2$ as an alkalinity source.

4.1.3 $Mg(OH)_2$: Slow dissolution and strong inhibition in high-salinity water

The performance of $Mg(OH)_2$ was strongly modulated by salinity, with high–salinity water causing a marked reduction in alkalinity delivery relative to the lower-salinity treatments. This response became more severe at 28°C, where net alkalinity loss was observed (Figs. 1 and A1c). While $Mg(OH)_2$ is less soluble than $Ca(OH)_2$, SI values indicate that bulk seawater also remained undersaturated (Rumble, 2021; Table B1). Hence, the observed patterns may be also linked to precipitation.

At salinities ≤ 34, while $Mg(OH)_2$ dissolved more slowly than $Ca(OH)_2$, it was more effective delivering the expected alkalinity (Figs. 1, A1c and A2c). At low temperature, greater CO_2 availability and stronger buffering help neutralize released OH^- and sustain dissolution. As temperature increases, CO_2 solubility and ingassing decline, slowing this neutralization and weakening the dissolution gradient. However, the absence of ΔTA plateaus indicates that dissolution remained continuous rather than being prematurely stopped, unlike $Ca(OH)_2$ under similar conditions.

At salinity 38, the system appears to surpass a threshold, leading to a sharp decline in alkalinity delivery (Fig. A1c). Although increasing salinity alters ion activities and may affect the apparent saturation state of brucite (Ayogu et al., 2020), any thermodynamic effect is likely offset by the rapid buildup of OH^- in the particle micro–environment. This can elevate pH and bring the system to local saturation earlier, favoring carbonate formation and thereby lowering net alkalinity release. As temperature rises, higher Ω_{Ar} and elevated Ca^{2+} and CO_3^{2-} activities further favor carbonate precipitation. Even when bulk Ω_{Ar} values remained moderate, sustained alkalinity release can generate much higher local saturation states within particle boundary layers, driving local precipitation under only modest bulk supersaturation (Figs. 1 and A3c). This could explain why runaway TA loss was observed under the most extreme T–S combinations (Moras et al., 2022)

Mg^{2+} is known to inhibit calcite nucleation and growth, increasing the nucleation energy barrier (Mucci, 1983; Pan et al., 2021). This mechanism could suppress widespread $CaCO_3$ precipitation at salinities ≤ 34. However, the results suggest that inhibition is not absolute. At sufficiently high temperature and salinity, the thermodynamic drive toward carbonate formation may strengthen to a point where it can overcome kinetic inhibition, facilitating heterogeneous precipitation on particle surfaces and potentially triggering runaway processes. Under such conditions, the diffusive boundary layer may reach carbonate saturation earlier than the bulk solution, effectively suppressing further dissolution at the particle surface.

Notably, the onset of precipitation in our warm and saline treatments occurred at bulk Ω_{Ar} values far lower than those reported in a study by Moras et al. (2024), with values near 9 (Fig. A3c). This discrepancy may be related to experimental setup: the more aggressive stirring used in that study (200 RPM) likely shortened the lifetime of particle microenvironments with elevated pH. In our experiment, weaker mixing may have allowed these interfacial zones to develop and persist long enough for heterogeneous nucleation to occur at the particle surface, even while the bulk solution remained only moderately supersaturated, consistent with Moras et al. (2026).

The decelerating dissolution trajectories observed in our results might be related to partial surface passivation (Fig. 3c). Although not conducted in seawater, both Harrison et al. (2015) and Hövelmann et al. (2012) showed that $Mg(OH)_2$ dissolution can trigger localized carbonate precipitation directly on particle surfaces. Such phases can form patchy coatings that reduce the effective reactive surface area without fully hindering dissolution, which aligns with the gradual, non-abrupt deceleration patterns observed in our experiments. This effect is expected to intensify at higher temperature and salinity, where local supersaturation is more persistent. Further support for this interpretation comes from Moras et al. (2024, 2026), who reported that $Mg(OH)_2$ particles acted as initial heterogeneous nucleation sites for $CaCO_3$, which then served as dominant nuclei for continued precipitation. These $CaCO_3$ precipitates may further develop into broccoli–like aggregates that retain undissolved $Mg(OH)_2$ cores, suggesting that passivation can be incomplete and transient rather than fully shutting down dissolution.

Thus, $Mg(OH)_2$ shows a distinct response from $Ca(OH)_2$. At low to moderate salinity and temperature, dissolution is slower but more continuous, with alkalinity delivery governed mainly by dissolution kinetics and the availability of CO_2 buffering. In contrast, high salinity combined with elevated temperature greatly increases the likelihood of local boundary–layer supersaturation, heterogeneous carbonate precipitation, and partial surface passivation, leading to strongly reduced or even negative net ΔTA gains.

4.2 Empirical Model Performance

The empirical parameterizations developed in this study fairly reproduce the dissolution-dominated phase of $NaHCO_3$, $Ca(OH)_2$ and $Mg(OH)_2$ across the tested T–S range. Scenarios showing net alkalinity loss were excluded from the parameter fits (e.g., $Ca(OH)_2$ at 28 °C, $Mg(OH)_2$ at $S = 38$); for those conditions, the model should be interpreted as describing the maximum achievable alkalinity release in the absence of precipitation–driven losses. The three fitted parameters provide a compact summary of alkalinity release dynamics under the tested conditions, indicating the magnitude (*a*), rate (*k*) and shape (β) of the alkalinity delivery curve over time. Although empirical, these parameters integrate all processes affecting alkalinity delivery under the experimental conditions and allow consistent comparison among materials and environments, showing the feasibility of translating material behavior into one function.

4.2.1 Interpretation of the empirical parameters

The parameter *a* defines the asymptotic value of the alkalinity–increment fraction, that is, the maximum potential alkalinity release predicted by f_A in the long term (Eq. 2). Because ΔTA integrates both material dissolution and precipitation processes, *a* reflects the effective alkalinity yield rather than a purely thermodynamic solubility limit. Overall, this parameter reflects the observed experimental results (Figs. 1 and 2). $NaHCO_3$ achieves values close to 1 in all cases, denoting full dissolution. $Ca(OH)_2$ shows lower values under warmer conditions, indicating that temperature is the dominant driver. For $Mg(OH)_2$, the parameter is strongly suppressed at high salinity. However, its values exceed the final observed ΔTA because the experiment had not yet reached the model asymptote; accordingly, the model predicts a larger ultimate alkalinity yield than was attained within the experimental duration.

The apparent rate constant *k* describes the speed at which the system approaches its asymptote, with larger values indicating a more rapid effect of alkalinity release (Fig. 2b). While *k* is not a mechanistic rate law for material dissolution, it reflects the combined influence of mineral reactivity, CO_2 buffering, mixing, and the changing chemical environment near the particles. For $NaHCO_3$, *k* was uniformly large, indicating a very rapid dissolution, independent of environmental conditions. $Ca(OH)_2$ showed a *k* mainly governed by temperature, with higher temperatures producing faster apparent dissolution. While this is kinetically expected, warmer conditions also promote precipitation, which reduces the net alkalinity gain. As a result, the lower plateaus are reached more rapidly. For $Mg(OH)_2$, *k* decreased with temperature and increased slightly with salinity, indicating stronger time–dependent inhibition under warmer and more saline conditions.

The curvature parameter β captures deviations from simple first-order kinetics. $\beta = 1$ corresponds to classical exponential behavior, as observed in $NaHCO_3$ and $Ca(OH)_2$. In contrast, $Mg(OH)_2$ required $\beta < 1$, with warmer seawater producing lower β values. This indicates increasingly decelerating release over time and is consistent with progressive deceleration or inhibition (Fig. 2).

4.3 Experimental limitations and interpretation

A limitation of this study is the absence of replicate experimental units, which prevents a direct quantification of bottle–to–bottle variability. However, the high–frequency sampling and technical replication of TA and DIC analyses provide confidence in the observed temporal patterns. In addition, the consistency of the response across the T–S matrix for the three materials supports the robustness of the identified kinetic trends. These results should therefore be interpreted as controlled mechanistic responses under these experimental conditions, rather than as universal estimates of material performance.

The experimental setup also differs from real ocean conditions. In particular, the experiments were conducted without dilution and at a relatively high particle–to–water interface, which likely prolonged local pH and carbonate gradients near dissolving particles and may have enhanced secondary precipitation. Moreover, the potential influence of the bottle walls could not be quantified and may have further promoted carbonate formation. Accordingly, the derived alkalinity–release parameters should be viewed as upper bounds under dissolution–dominated conditions, with precipitation losses causing downward deviations from these values.

4.3.1 Implications for MRV and biological links

This dataset shows that in a bottle system with intermittent headspace exposure during sampling, the apparent evolution of ΔTA and ΔDIC can reflect different processes over time. For MRV, this matters because a rise in ΔTA does not necessarily imply complete retention of net alkalinity gain: precipitation losses and air–sea CO_2 exchange can act on different timescales, and CO_2 ingassing can partially mask the DIC reduction from secondary $CaCO_3$ precipitation (Ho et al., 2023; Moras et al., 2026). In consequence, modest or transient changes in ΔDIC do not necessarily indicate the absence of precipitation losses, even when ΔTA clearly shows reduced alkalinity delivery. This implies that DIC alone is not a unique indicator of alkalinity–loss processes under ongoing air–sea gas exchange. TA remains the primary indicator of net alkalinity gain, ideally supported by pH, pCO_2, and constraints on exchange and mixing.

Furthermore, in this experiment, Ω_{Ar} is evaluated for the bulk solution and cannot be directly measured at the dissolving particle interface. However, because boundary–layer pH and carbonate formation are expected to be strongest when bulk Ω_{Ar} peaks are high and persistent, bulk Ω_{Ar} dynamics can be used as an empirical proxy for local precipitation susceptibility. Under stronger dilution and faster mixing, the residence time of these interfacial gradients would be reduced, and the inferred precipitation risk would likely decrease (Suitner et al., 2024). Thus, considering the studied materials, the use of particles in OAE implementation would likely achieve the most potential under colder and less saline environments, while in warmer and saltier conditions it would generally benefit from stronger mixing and advective renewal (Flipkens et al., 2023).

From a biological perspective, this MRV point is also relevant. Even when net alkalinity gain appears stable, hydroxide dissolution can still generate transient local high–pH exposure and localized carbonate–system perturbations near dissolving particles. Ecological outcomes may therefore depend not only on the eventual bulk chemical state, but also consider the intensity and duration of these excursions. Mesocosm and toxicity studies to date suggest that ecological sensitivity varies strongly with the type of alkalinity perturbation, the magnitude of local extremes, and the ecosystem context. For $NaHCO_3$, comparable additions indicate low ecosystem sensitivity under this CO_2–equilibrated conditions (e.g., Xin et al., 2024; Gropelli et al., 2026). For hydroxides, effects appear more likely when perturbations are strong, transient, or oversaturated, which is precisely the regime where our time–series indicate that precipitation feedbacks and carbonate–system instability can develop (Antoni et al., 2025). In particular, Delacroix et al. (2023, 2024) reported ecological effects that depend on how and how fast local extremes are produced and indicated comparatively lower acute toxicity for $Mg(OH)_2$ relative to $Ca(OH)_2$.

4.3.2 Conservative material performance and model applicability

Taken together, the results indicate that material performance is strongly context dependent. This emphasizes that OAE feedstocks should not be chosen solely by added mass or nominal alkalinity content. Instead, their effective alkalinity yield depends on the environmental regime in which they are deployed. In this sense, the 500 µmol kg^{-1} addition provides a useful test dose for identifying where each material remains dissolution–dominated and where precipitation losses become important under our experimental constraints. It delineates where each material is likely to perform well, where performance may become unstable, and where precipitation risk increases. Similarly, the empirical parameterizations developed here are not intended as literal predictions of open–ocean deployment, but as conservative boundaries for assessing potential performance solely considering temperature and salinity, and they can be used as screening tools in OAE planning frameworks to compare material behavior across environments (Bach et al., 2025; Fig. 4).

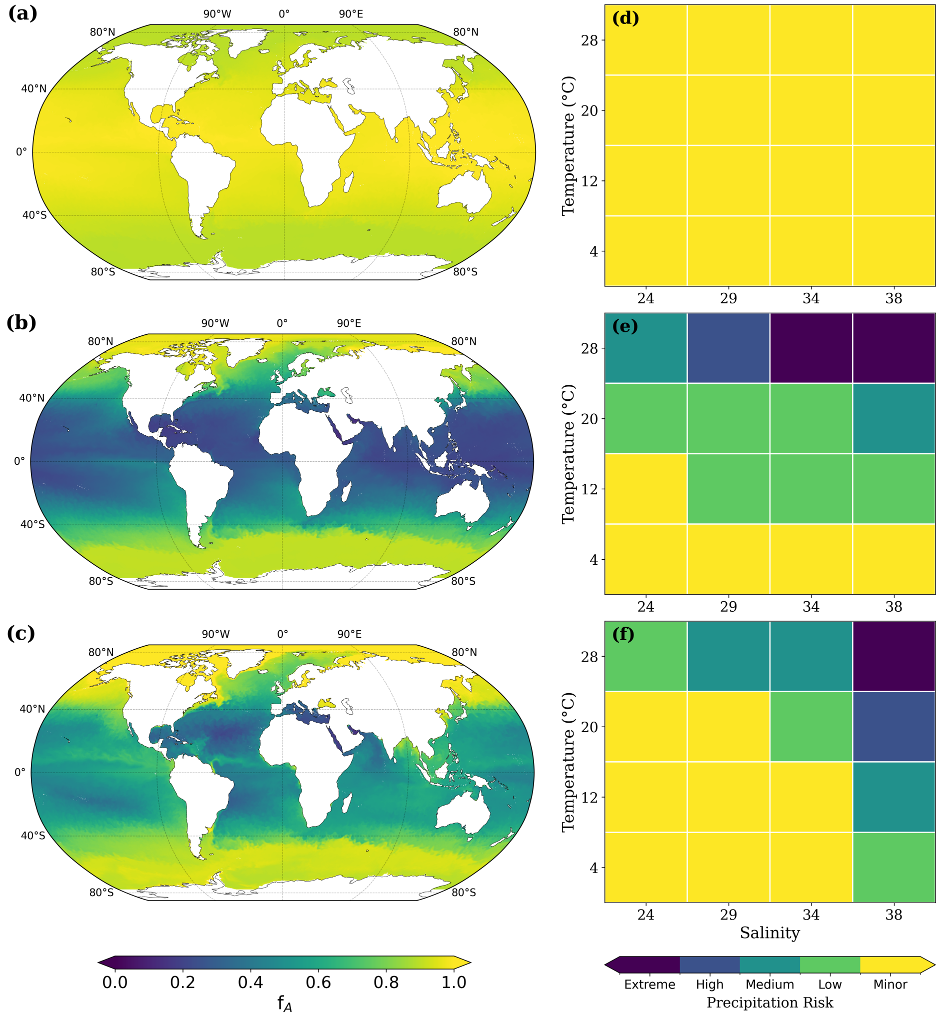

https://doi.org/10.5194/egusphere-2026-3277
Preprint. Discussion started: 29 June 2026

Figure 4. Left: fitted asymptotic alkalinity fraction for (a) $NaHCO_3$, (b) $Ca(OH)_2$, and (c) $Mg(OH)_2$, calculated from Copernicus sea–surface temperature and salinity fields for October 2025. The maps provide a conservative first–order indication of where each material is expected to deliver its highest potential alkalinity. Right: potential precipitation risk based on the experimental results for (d) $NaHCO_3$, (e) $Ca(OH)_2$, and (f) $Mg(OH)_2$ (see Fig. A1). Colors indicate risk classes derived from the last measured ΔTA (μmol kg^{-1}): Extreme (<0), High (0–100), Medium (100–250), Low (250–400), and Minor (400–500).

The above distinctions are important for interpretation. Real ocean deployment would involve stronger dilution, more variable mixing, larger water renewal, and faster air–sea gas exchange than in the present bottles. These processes would generally reduce the residence time of high–pH boundary layers and may therefore decrease the precipitation feedbacks observed here. At the same time, additional factors not represented in the experiment (such as particle size distribution, aggregation, sinking, turbulence, and deployment strategy) would further shape the outcome. Future work should therefore incorporate explicit precipitation kinetics, particle–size effects, and mixing–dependent transport into more process–based models (Bianchi et al., 2024; Shaw et al., 2025; Suitner et al., 2024).

5. Conclusion

This study provides a systematic experimental assessment of how temperature and salinity regulate the dissolution behavior and effective alkalinity delivery of three widely discussed OAE feedstocks. Across 16 temperature–salinity combinations, we show that these environmental variables are first–order controls on net alkalinity delivery. Their effects operate through coupled changes in carbonate chemistry, CO_2 availability, and interfacial precipitation processes, with important implications for the efficiency, stability, and predictability of OAE.

$NaHCO_3$ dissolved rapidly and predictably across all tested scenarios, showing little sensitivity to temperature or salinity. $Ca(OH)_2$ delivered high alkalinity in cold waters, but its efficiency declined under warmer and more saline conditions where precipitation feedbacks became increasingly important. $Mg(OH)_2$ dissolved more slowly and was especially sensitive to high salinity, with strong suppression only emerging under the warmest and most saline conditions. Together, these results indicate that feedstock performance is highly context dependent and that regional deployment strategies should account for the environmental conditions most likely to favor stable alkalinity delivery.

Building on these observations, we derived empirical dissolution parameterizations based on a modified Noyes–Whitney formulation, expressing the effective alkalinity fraction as a function of temperature, salinity, and time. The fitted parameters capture the magnitude, rate, and shape of net alkalinity delivery under dissolution–dominated conditions.

As the experiments were conducted in bottles without particle sinking nor dilution, the present results should be viewed as conservative boundaries rather than general predictions for open–ocean deployment. Future experiments should therefore include explicit transport and mixing effects, sinking particles, and more process–resolving treatments of precipitation and gas exchange to refine these parameterizations. Such studies, together with mesocosm and in situ validation, will be needed to improve prediction of alkalinity release under realistic deployment scenarios. Despite this, the study provides a first step towards bridging laboratory experiment and modeling, serving as a reference for deployment planning and MRV.

Data Availability

The data will be made available in a public repository upon acceptance of the manuscript for publication.

Author Contributions

MSM and CAM designed the study. MSM conducted the experiments. MSM and PB performed the analyses. MSM drafted the manuscript, with input from CAM. JH, JB, and PB provided additional input. All authors reviewed and approved the final version of the manuscript. Funding acquisition was secured by JH.

Competing Interests

JH is consulting for the Planeteers GmbH. All authors declare that they have no competing interests.

Acknowledgments

The authors acknowledge the use of AI-assisted tools for literature search. All relevant output was subsequently checked and reviewed by the authors before incorporation into the manuscript.

Financial Support

This research has been supported by the Ocean Alk–Align project funded by the Carbon to Sea Initiative, and by the German Federal Ministry of Education and Research through the CDRmare project RETAKE–II (grant no 03F0965F).

Appendix A

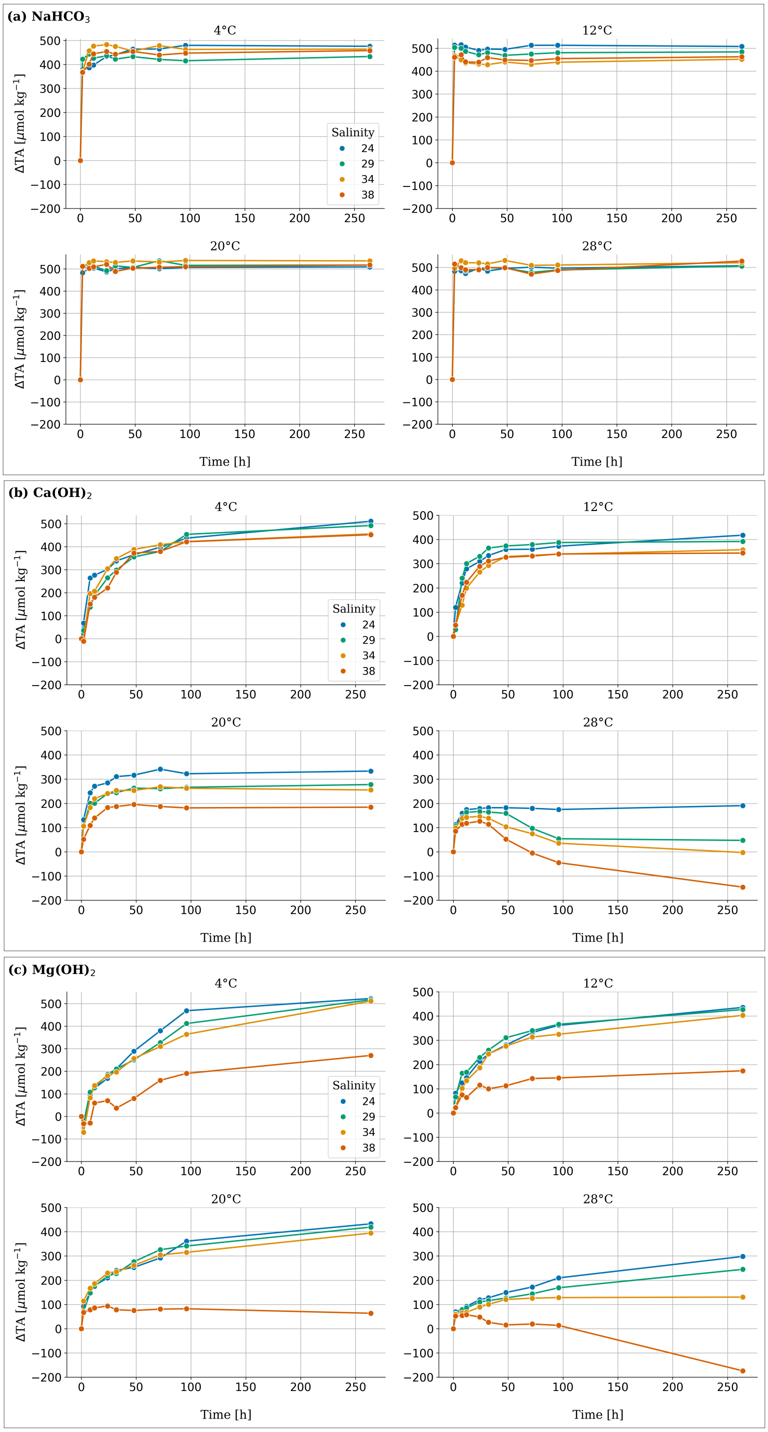

Figure A1: ΔTA time series over 264 hours for (a) NaHCO$_3$, (b) Ca(OH)$_2$, and (c) Mg(OH)$_2$ at the four investigated temperatures. Salinity levels are indicated by color. All plots use the same scale to facilitate comparison.

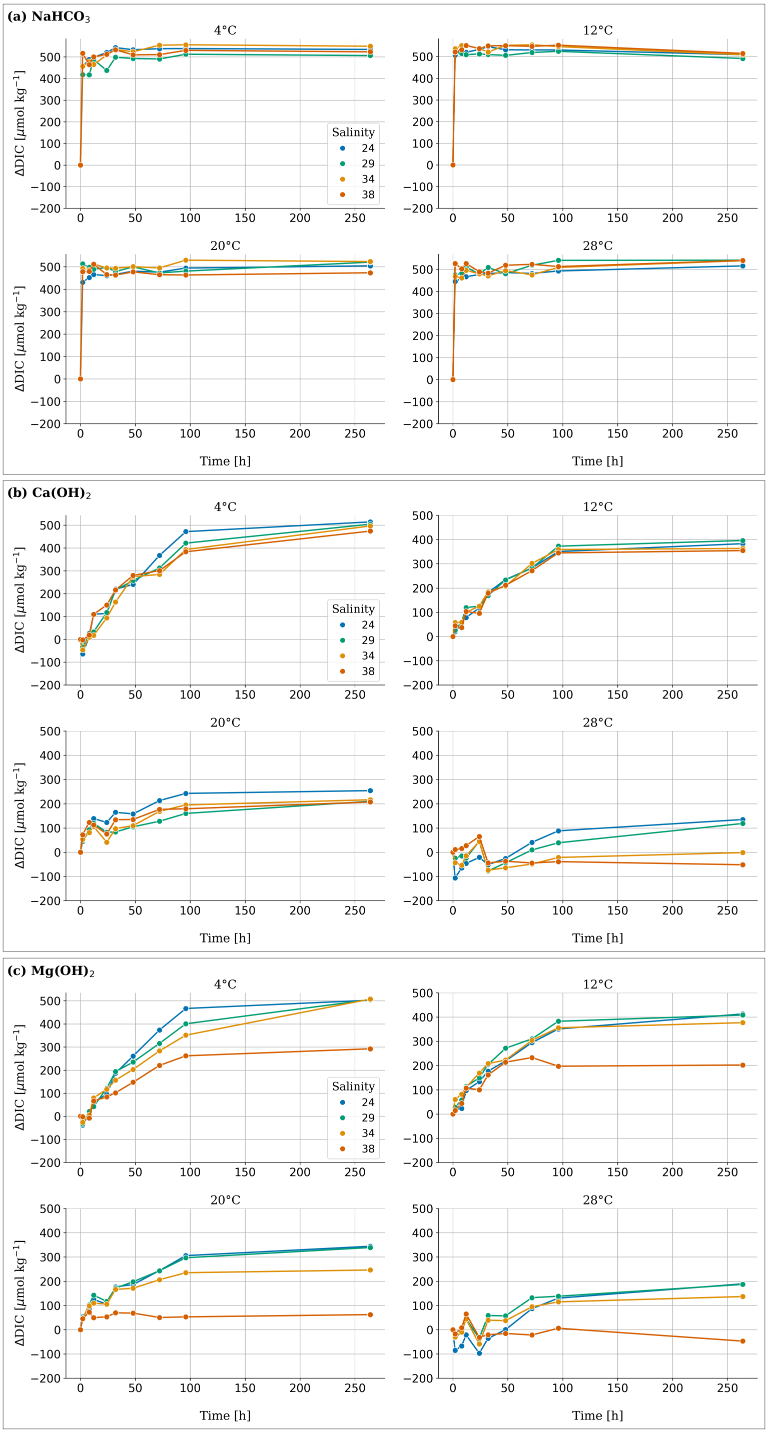

Figure A2: ΔDIC time series for (a) $NaHCO_3$, (b) $Ca(OH)_2$, and (c) $Mg(OH)_2$ over 264 hours at the four studied temperatures. Salinity levels are indicated by color. All plots use the same scale to facilitate comparison.

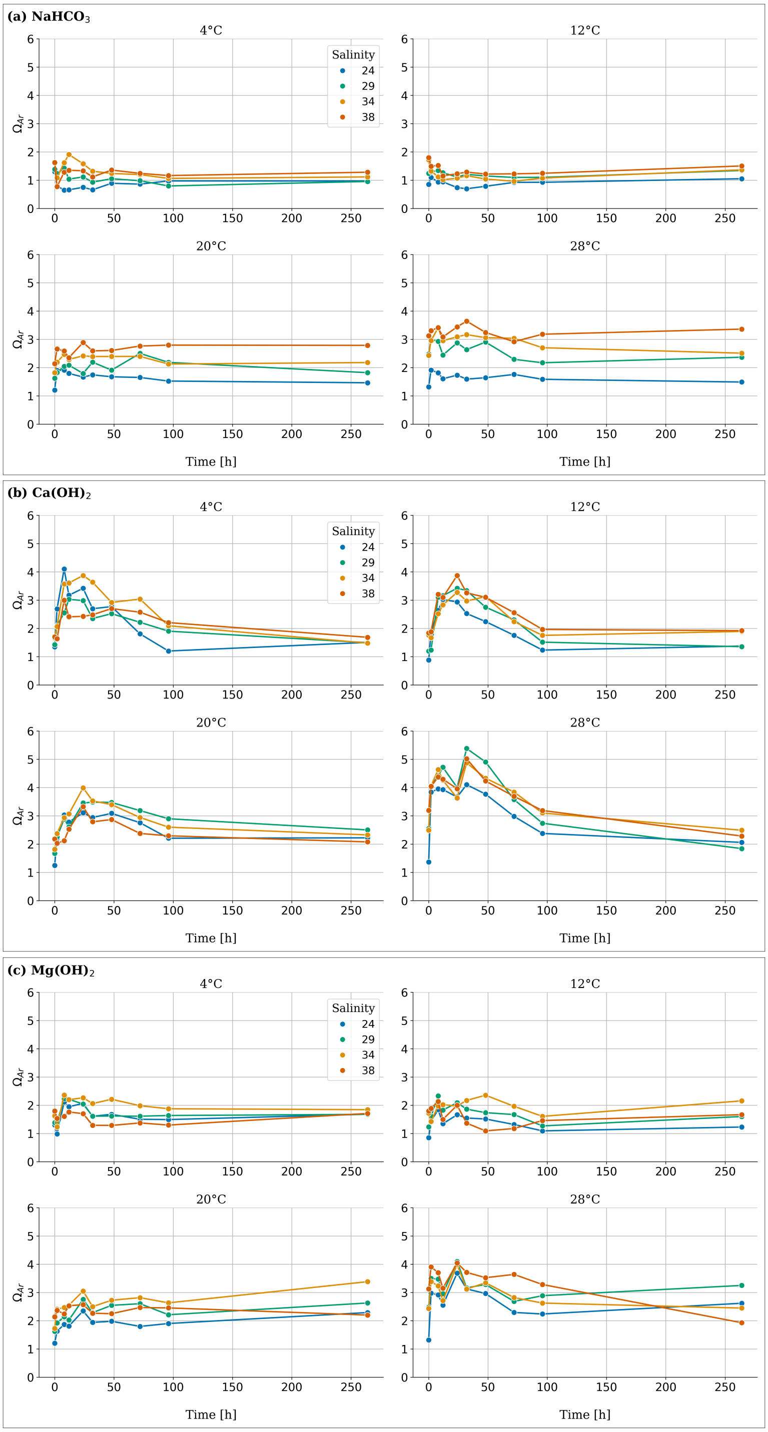

Figure A3: Ω_{Ar} time series for (a) $NaHCO_3$, (b) $Ca(OH)_2$, and (c) $Mg(OH)_2$ over 264 hours at the four studied temperatures. Salinity levels are indicated by color. All plots use the same scale to facilitate comparison.

https://doi.org/10.5194/egusphere-2026-3277
Preprint. Discussion started: 29 June 2026

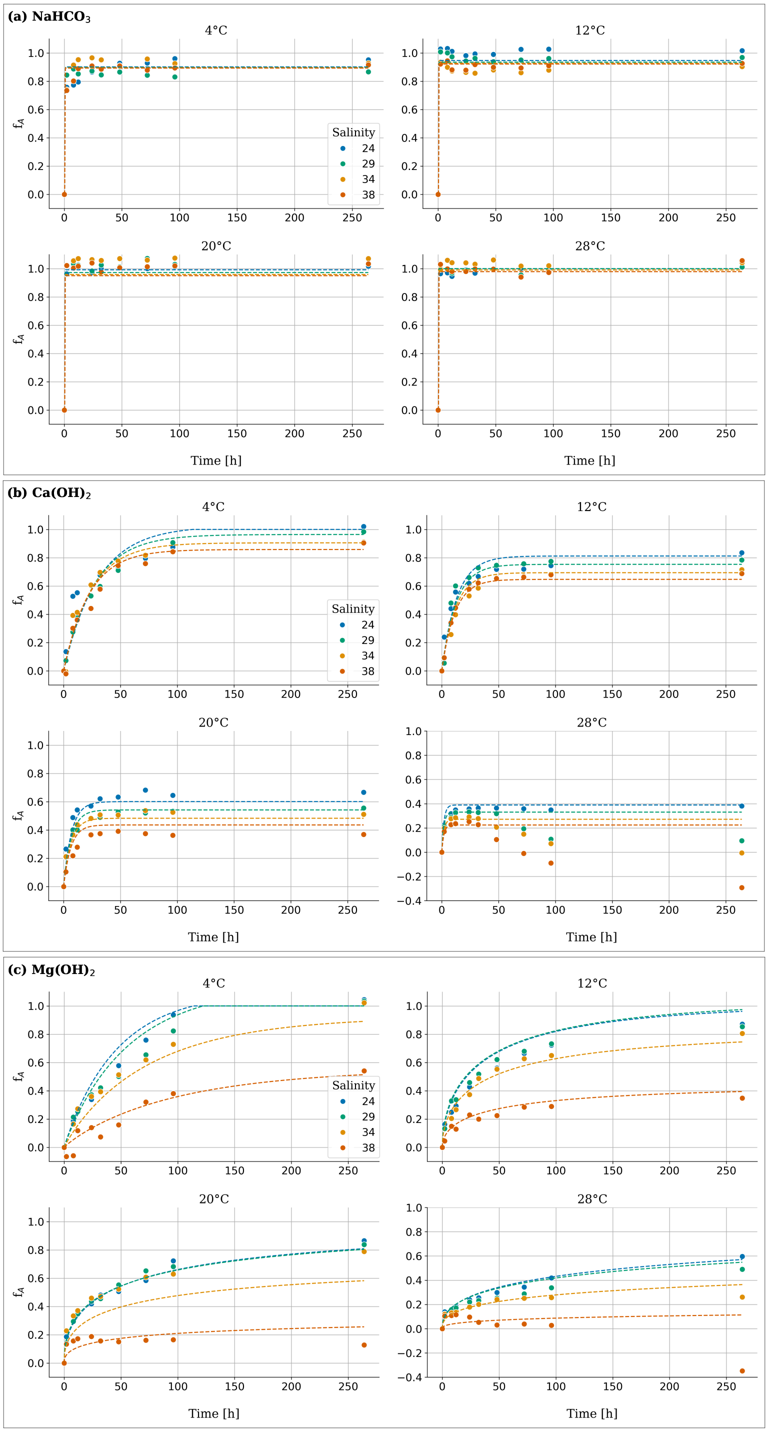

Figure A4: Modelled alkalinity function f_A time series over 264 hours for (a) NaHCO$_3$, (b) Ca(OH)$_2$, and (c) Mg(OH)$_2$ at the four studied temperatures. Salinity levels are indicated by color.

Appendix B

Table B1: SI at equilibrium after an alkalinity addition of 500 µmol kg^{-1} under the studies conditions for the three materials.

Temperature (°C)	Salinity	$NaHCO_3$	$Ca(OH)_2$	$Mg(OH)_2$
4	**24**	-2.89	-8.77	-1.86
4	**29**	-2.77	-9.04	-2.13
4	**34**	-2.66	-9.25	-2.32
4	**38**	-2.59	-9.41	-2.48
12	**24**	-2.96	-8.40	-1.68
12	**29**	-2.84	-8.61	-1.88
12	**34**	-2.74	-8.75	-2.03
12	**38**	-2.66	-8.90	-2.17
20	**24**	-3.05	-7.93	-1.40
20	**29**	-2.93	-8.12	-1.59
20	**34**	-2.83	-8.33	-1.80
20	**38**	-2.75	-8.46	-1.91
28	**24**	-3.14	-7.57	-1.22
28	**29**	-3.13	-7.65	-1.29
28	**34**	-2.93	-7.91	-1.55
28	**38**	-2.85	-7.91	-1.54

Table B2: SI at equilibrium for aragonite and calcite after the alkalinity additions under all conditions for the three materials.

		$NaHCO_3$		$Ca(OH)_2$		$Mg(OH)_2$	
Temperature (°C)	**Salinity**	**Aragonite**	**Calcite**	**Aragonite**	**Calcite**	**Aragonite**	**Calcite**
4	**24**	0.08	0.23	0.92	1.08	0.94	1.08
4	**29**	0.11	0.25	0.94	1.10	0.93	1.08
4	**34**	0.17	0.32	0.95	1.10	0.94	1.09
4	**38**	0.19	0.34	0.95	1.10	0.94	1.08
12	**24**	0.04	0.21	0.92	1.08	0.91	1.07
12	**29**	0.10	0.26	0.94	1.10	0.93	1.09
12	**34**	0.22	0.38	0.96	1.12	0.95	1.11
12	**38**	0.25	0.41	0.96	1.12	0.95	1.11
20	**24**	0.03	0.21	0.94	1.11	0.92	1.10
20	**29**	0.15	0.32	0.96	1.13	0.94	1.12
20	**34**	0.20	0.37	0.96	1.13	0.94	1.12
20	**38**	0.26	0.44	0.97	1.14	0.96	1.13
28	**24**	0.03	0.22	0.94	1.13	0.92	1.11
28	**29**	0.26	0.45	0.96	1.15	0.95	1.17
28	**34**	0.26	0.46	0.99	1.18	0.97	1.14
28	**38**	0.43	0.62	1.02	1.22	1.01	1.21

Table B3: AIC analysis for the models using $\beta = 1$ and $\beta \neq 1$ across conditions for the three materials and all studied conditions.

		$NaHCO_3$		$Ca(OH)_2$		$Mg(OH)_2$	
Temperature (°C)	**Salinity**	$\beta = 1$	$\beta \neq 1$	$\beta = 1$	$\beta \neq 1$	$\beta = 1$	$\beta \neq 1$
4	**24**	-47,936	-48,713	-47,936	-48,713	-47,936	-48,713
4	**29**	-65,758	-61,473	-65,758	-61,473	-65,758	-61,473
4	**34**	-50,119	-72,401	-50,119	-72,401	-50,119	-72,401
4	**38**	-52,645	-69,364	-52,645	-69,364	-52,645	-69,364
12	**24**	-97,159	-92,873	-97,159	-92,873	-97,159	-92,873
12	**29**	-72,769	-68,484	-72,769	-68,484	-72,769	-68,484
12	**34**	-62,671	-58,386	-62,671	-58,386	-62,671	-58,386
12	**38**	-72,975	-68,689	-72,975	-68,689	-72,975	-68,689
20	**24**	-81,693	-77,407	-81,693	-77,407	-81,693	-77,407
20	**29**	-101,420	-97,134	-101,420	-97,134	-101,420	-97,134
20	**34**	-205,391	-210,933	-205,391	-210,933	-205,391	-210,933
20	**38**	-93,694	-89,409	-93,694	-89,409	-93,694	-89,409
28	**24**	-75,916	-71,630	-75,916	-71,630	-75,916	-71,630
28	**29**	-79,069	-74,783	-79,069	-74,783	-79,069	-74,783
28	**34**	-119,505	-115,219	-119,505	-115,219	-119,505	-115,219
28	**38**	-75,074	-70,788	-75,074	-70,788	-75,074	-70,788

Table B4: R^2 and RSME for all the treatments.

		$NaHCO_3$		$Ca(OH)_2$		$Mg(OH)_2$	
Temperature (°C)	**Salinity**	R^2	**RMSE**	R^2	**RMSE**	R^2	**RMSE**
4	**24**	0.924	0.075	0.806	0.132	0.929	0.099
4	**29**	0.971	0.044	0.963	0.062	0.913	0.097
4	**34**	0.947	0.065	0.966	0.059	0.922	0.092
4	**38**	0.942	0.063	0.962	0.061	0.915	0.056
12	**24**	0.948	0.070	0.912	0.073	0.894	0.084
12	**29**	0.975	0.046	0.950	0.063	0.933	0.066
12	**34**	0.966	0.049	0.967	0.045	0.969	0.043
12	**38**	0.993	0.023	0.992	0.022	0.894	0.034
20	**24**	0.996	0.018	0.915	0.060	0.980	0.034
20	**29**	0.967	0.056	0.954	0.036	0.990	0.024
20	**34**	0.905	0.098	0.942	0.040	0.578	0.138
20	**38**	0.956	0.064	0.762	0.063	0.432	0.060
28	**24**	0.993	0.025	0.914	0.038	0.899	0.027
28	**29**	0.996	0.020	0.981	0.016	0.817	0.033
28	**34**	0.978	0.046	0.983	0.014	0.884	0.022
28	**38**	0.987	0.034	0.969	0.015	0.853	0.056

References

Akaike, H.: Factor analysis and AIC, Psychometrika, 52, 317–332, https://doi.org/10.1007/BF02294359, 1987.

Antoni, D., Wichels, A., Boersma, M., and Gerdts, G.: The effect of ocean alkalinity enhancement on pelagic bacterial communities: focus points derived from a mesocosm experiment, Front. Microbiomes, 4, 1606890, https://doi.org/10.3389/frmbi.2025.1606890, 2025.

Ayogu, P. C., Ezugwu, M. I., and Eze, F. I.: Principle of Common-ion Effect and its Application in Chemistry: a Review. Journal of Chemistry Letters, 1(2), 77-83, 2020.

Bach, L. T., Tyka, M. D., Wang, B., and Fennel, K.: Lethal by design? Guiding environmental assessments of ocean alkalinity enhancement toward realistic contextualization of the alkalinity perturbation, CDRXIV, 10.70212/cdrxiv.2025457.v1, 2025.

Bianchi, R., Abbate, S., Lockley, A., Abbà, A., Campo, F., Varliero, S., Grosso, M., and Caserini, S.: Evaluating rainbowing for ocean alkalinity enhancement, Environ. Res. Commun., 6, 095003, https://doi.org/10.1088/2515-7620/ad707b, 2024.

Delacroix, S., Nystuen, T. J., Höglund, E., and King, A. L.: Biological impact of ocean alkalinity enhancement of magnesium hydroxide on marine microalgae using bioassays simulating ship-based dispersion, https://doi.org/10.5194/bg-2023-138, 17 August 2023.

Delacroix, S., Nystuen, T. J., Tobiesen, A. E. D., King, A. L., and Höglund, E.: Ocean alkalinity enhancement impacts: regrowth of marine microalgae in alkaline mineral concentrations simulating the initial concentrations after ship-based dispersions, Biogeosciences, 21, 3677–3690, https://doi.org/10.5194/bg-21-3677-2024, 2024.

Dickson, A. G.: Standard potential of the reaction: AgCl(s) + ½ H2(g) = Ag(s) + HCl(aq), and the standard acidity constant of the ion $HSO4^-$ in synthetic sea water from 273.15 to 318.15 K, The Journal of Chemical Thermodynamics, 22, 113–127, https://doi.org/10.1016/0021-9614(90)90074-Z, 1990.

Dickson, A. G. and Riley, J. P.: The estimation of acid dissociation constants in seawater media from potentionmetric titrations with strong base. I. The ionic product of water – Kw, Marine Chemistry, 7, 89–99, https://doi.org/10.1016/0304-4203(79)90001-X, 1979.

Dickson, A. G., Sabine, C. L., Christian, J. R., and M: Guide to best practices for ocean CO2 measurements., North Pacific Marine Science Organization, 2007.

Dokoumetzidis, A., Papadopoulou, V., and Macheras, P.: Analysis of Dissolution Data Using Modified Versions of Noyes–Whitney Equation and the Weibull Function, Pharm Res, 23, 256–261, https://doi.org/10.1007/s11095-006-9093-3, 2006.

Eisaman, M. D., Geilert, S., Renforth, P., Bastianini, L., Campbell, J., Dale, A. W., Foteinis, S., Grasse, P., Hawrot, O., Löscher, C. R., Rau, G. H., and Rønning, J.: Assessing the technical aspects of ocean-alkalinity-enhancement approaches, State of the Planet, 2-oae2023, 1–29, https://doi.org/10.5194/sp-2-oae2023-3-2023, 2023.

Flipkens, G., Fuhr, M., Fiers, G., Meysman, F. J. R., Town, R. M., and Blust, R.: Enhanced olivine dissolution in seawater through continuous grain collisions, Geochimica et Cosmochimica Acta, 359, 84-99, 10.1016/j.gca.2023.09.002, 2023.

Friedlingstein, P., O'Sullivan, M., Jones, M. W., Andrew, R. M., Hauck, J., Landschützer, P., Le Quéré, C., Li, H., Luijkx, I. T., Olsen, A., Peters, G. P., Peters, W., Pongratz, J., Schwingshackl, C., Sitch, S., Canadell, J. G., Ciais, P., Jackson, R. B., Alin, S. R., Arneth, A., Arora, V., Bates, N. R., Becker, M., Bellouin, N., Berghoff, C. F., Bittig, H. C., Bopp, L., Cadule, P., Campbell, K., Chamberlain, M. A., Chandra, N., Chevallier, F., Chini, L. P., Colligan, T., Decayeux, J., Djeutchouang, L. M., Dou, X., Duran Rojas, C., Enyo, K., Evans, W., Fay, A. R., Feely, R. A., Ford, D. J., Foster, A., Gasser, T., Gehlen, M., Gkritzalis, T., Grassi, G., Gregor, L., Gruber, N., Gürses, Ö., Harris, I., Hefner, M., Heinke, J., Hurtt, G. C., Iida, Y., Ilyina, T., Jacobson, A. R., Jain, A. K., Jarníková, T., Jersild, A., Jiang, F., Jin, Z., Kato, E., Keeling, R. F., Klein Goldewijk, K., Knauer, J., Korsbakken, J. I., Lan, X., Lauvset, S. K., Lefèvre, N., Liu, Z., Liu, J., Ma, L., Maksyutov, S., Marland, G., Mayot, N., McGuire, P. C., Metzl, N., Monacci, N. M., Morgan, E. J., Nakaoka, S.-I., Neill, C., Niwa, Y., Nützel, T., Olivier, L., Ono, T., Palmer, P. I., Pierrot, D., Qin, Z., Resplandy, L., Roobaert, A., Rosan, T. M., Rödenbeck, C., Schwinger, J., Smallman, T. L., Smith, S. M., Sospedra-Alfonso, R., Steinhoff, T., et al.: Global Carbon Budget 2024, Earth Syst. Sci. Data, 17, 965–1039, https://doi.org/10.5194/essd-17-965-2025, 2025.

Gagern, A., Manley, J., Kapsenberg, L., and J, L.: Ocean-Based Carbon Dioxide Removal: A New Frontier in the Blue Economy, Marine Technology Society Journal, 56, 40–48, https://doi.org/10.4031/mtsj.56.1.15, 2022.

Goldsmith, J. A., Randall, N., and Ross, S. D.: On methods of expressing dissolution rate data, J Pharm Pharmacol, 30, 347–349, https://doi.org/10.1111/j.2042-7158.1978.tb13253.x, 1978.

Groppelli, S., Calvi, D., Comazzi, F., Alamooti, S. J., Azzellino, A., Barbaccia, E., Caronni, S., Macchi, P., Raos, G., and Basso, D.: The response of phytoplankton to pH-equilibrated ocean alkalinization: A mesocosm experiment with harbour waters, Marine Pollution Bulletin, 222, 118787, https://doi.org/10.1016/j.marpolbul.2025.118787, 2026.

Harrison, A. L., Dipple, G. M., Power, I. M., and Mayer, K. U.: Influence of surface passivation and water content on mineral reactions in unsaturated porous media: Implications for brucite carbonation and CO2 sequestration, Geochimica et Cosmochimica Acta, 148, 477–495, https://doi.org/10.1016/j.gca.2014.10.020, 2015.

Hartmann, J., Suitner, N., Lim, C., Schneider, J., Marín-Samper, L., Arístegui, J., Renforth, P., Taucher, J., and Riebesell, U.: Stability of alkalinity in ocean alkalinity enhancement (OAE) approaches – consequences for durability of CO2 storage, Biogeosciences, 20, 781–802, https://doi.org/10.5194/bg-20-781-2023, 2023.

Hashim, M. S., Marx, L., Klein, F., Dean, C. L., Burdige, E., Hayden, M., McCorkle, D. C., and Subhas, A. V.: Mineral formation during shipboard ocean alkalinity enhancement experiments in the North Atlantic, Biogeosciences, 22, 7149–7165, https://doi.org/10.5194/bg-22-7149-2025, 2025.

Ho, D. T., Bopp, L., Palter, J. B., Long, M. C., Boyd, P., Neukermans, G., & Bach, L. (2023). Monitoring, reporting, and verification for ocean alkalinity enhancement. State of the Planet Discussions, 2023, 1-15.

Hövelmann, J., Putnis, C. V., Ruiz-Agudo, E., and Austrheim, H.: Direct Nanoscale Observations of CO2 Sequestration during Brucite [Mg(OH)2] Dissolution, Environ. Sci. Technol., 46, 5253–5260, https://doi.org/10.1021/es300403n, 2012.

Humphreys, M. P., Lewis, E. R., Sharp, J. D., and Pierrot, D.: PyCO2SYS v1.8: marine carbonate system calculations in Python, Geoscientific Model Development, 15, 15–43, https://doi.org/10.5194/gmd-15-15-2022, 2022.

Ilyina, T., Wolf-Gladrow, D., Munhoven, G., and Heinze, C.: Assessing the potential of calcium-based artificial ocean alkalinization to mitigate rising atmospheric CO2 and ocean acidification, Geophysical Research Letters, 40, 5909–5914, https://doi.org/10.1002/2013GL057981, 2013.

IPCC: IPCC Climate Change 2023: synthesis report, edited by: Lee, H. and Romero, J., Intergovernmental Panel on Climate Change, Geneva, Switzerland, 169 pp., 2023.

Kheshgi, H. S.: Sequestering atmospheric carbon dioxide by increasing ocean alkalinity, Energy, 20, 915–922, https://doi.org/10.1016/0360-5442(95)00035-F, 1995.

Lueker, T. J., Dickson, A. G., and Keeling, C. D.: Ocean pCO2 calculated from dissolved inorganic carbon, alkalinity, and equations for K1 and K2: validation based on laboratory measurements of CO2 in gas and seawater at equilibrium, Marine Chemistry, 70, 105–119, https://doi.org/10.1016/S0304-4203(00)00022-0, 2000.

Marion, G. M., Millero, F. J., and Feistel, R.: Precipitation of solid phase calcium carbonates and their effect on application of seawater S_A-T-P models, Ocean Science, 5, 285–291, https://doi.org/10.5194/os-5-285-2009, 2009.

Millero, F. J., Feistel, R., Wright, D. G., and McDougall, T. J.: The composition of Standard Seawater and the definition of the Reference-Composition Salinity Scale, Deep Sea Research Part I: Oceanographic Research Papers, 55, 50–72, https://doi.org/10.1016/j.dsr.2007.10.001, 2008.

Moras, C. A., Bach, L. T., Cyronak, T., Joannes-Boyau, R., and Schulz, K. G.: Ocean alkalinity enhancement – avoiding runaway $CaCO_3$ precipitation during quick and hydrated lime dissolution, Biogeosciences, 19, 3537–3557, https://doi.org/10.5194/bg-19-3537-2022, 2022.

Moras, C. A., Bach, L. T., Cyronak, T., Joannes-Boyau, R., and Schulz, K. G.: Preparation and quality control of in-house reference materials for marine dissolved inorganic carbon and total alkalinity measurements, Limnology and Oceanography: Methods, 21(11), 637–644, https://doi.org/10.1002/lom3.10570, 2023.

Moras, C. A., Cyronak, T., Bach, L. T., Joannes-Boyau, R., and Schulz, K. G.: Effects of grain size and seawater salinity on magnesium hydroxide dissolution and secondary calcium carbonate precipitation kinetics: implications for ocean alkalinity enhancement, Biogeosciences, 21, 3463–3475, https://doi.org/10.5194/bg-21-3463-2024, 2024.

Moras, C. A., Saez Moreno, M., Bartsch, P., and Hartmann, J.: Impacts of water advection and CO2 exchanges on the carbon dioxide removal potential of ocean alkalinity enhancement, EGUsphere, 1–28, https://doi.org/10.5194/egusphere-2025-6144, 2026a.

Morse, J. W. and Arvidson, R. S.: The dissolution kinetics of major sedimentary carbonate minerals, Earth-Science Reviews, 58, 51–84, https://doi.org/10.1016/S0012-8252(01)00083-6, 2002.

Morse, J. W. and He, S.: Influences of T, S and PCO2 on the pseudo-homogeneous precipitation of CaCO3 from seawater: implications for whiting formation, Marine Chemistry, 41, 291–297, https://doi.org/10.1016/0304-4203(93)90261-L, 1993.

Morse, J. W., Arvidson, R. S., and Lüttge, A.: Calcium Carbonate Formation and Dissolution, Chem. Rev., 107, 342–381, https://doi.org/10.1021/cr050358j, 2007.

Mucci, A.: The solubility of calcite and aragonite in seawater at various salinities, temperatures, and one atmosphere total pressure, American Journal of Science, 283, 780–799, https://doi.org/10.2475/ajs.283.7.780, 1983.

Noyes, A. A. and Whitney, W. R.: THE RATE OF SOLUTION OF SOLID SUBSTANCES IN THEIR OWN SOLUTIONS., J. Am. Chem. Soc., 19, 930–934, https://doi.org/10.1021/ja02086a003, 1897.

Oschlies, A., Bach, L. T., Rickaby, R. E. M., Satterfield, T., Webb, R., and Gattuso, J.-P.: Climate targets, carbon dioxide removal, and the potential role of ocean alkalinity enhancement, State of the Planet, 2-oae2023, 1–9, https://doi.org/10.5194/sp-2-oae2023-1-2023, 2023.

Pan, Y., Li, Y., Ma, Q., He, H., Wang, S., Sun, Z., Cai, W.-J., Dong, B., Di, Y., Fu, W., and Chen, C.-T. A.: The role of Mg2+ in inhibiting CaCO3 precipitation from seawater, Marine Chemistry, 237, 104036, https://doi.org/10.1016/j.marchem.2021.104036, 2021.

Parkhurst, D. and Appelo, C. A. J.: Description of input and examples for PHREEQC version 3: A computer program for speciation, batch-reaction, one-dimensional transport, and inverse geochemical calculations, Reston, VA, https://doi.org/10.3133/tm6A43, 2013.

Renforth, P. and Henderson, G.: Assessing ocean alkalinity for carbon sequestration, Reviews of Geophysics, 55, 636–674, https://doi.org/10.1002/2016RG000533, 2017.

Ruiz-Agudo, E., Kudłacz, K., Putnis, C. V., Putnis, A., and Rodriguez-Navarro, C.: Dissolution and carbonation of Portlandite [Ca(OH)2] single crystals, Environ Sci Technol, 47, 11342–11349, https://doi.org/10.1021/es402061c, 2013.

Rumble, J. R. (Ed.): CRC handbook of chemistry and physics, 102nd edition 2021-2022., CRC Press, Boca Raton London New York, 1 pp., 2021.

Santinelli, C., Valsecchi, S., Retelletti Brogi, S., Bachi, G., Checcucci, G., Guerrazzi, M., Camatti, E., Caserini, S., Azzellino, A., and Basso, D.: Ocean liming effects on dissolved organic matter dynamics, Biogeosciences, 21, 5131–5141, https://doi.org/10.5194/bg-21-5131-2024, 2024.

Shaw, C., Ringham, M. C., Carter, B. R., Tyka, M. D., and Eisaman, M. D.: Using magnesium hydroxide for ocean alkalinity enhancement: elucidating the role of formation conditions on material properties and dissolution kinetics, Front. Clim., 7, 1616362, https://doi.org/10.3389/fclim.2025.1616362, 2025.

Suitner, N., Faucher, G., Lim, C., Schneider, J., Moras, C. A., Riebesell, U., and Hartmann, J.: Ocean alkalinity enhancement approaches and the predictability of runaway precipitation processes: results of an experimental study to determine critical alkalinity ranges for safe and sustainable application scenarios, Biogeosciences, 21, 4587–4604, https://doi.org/10.5194/bg-21-4587-2024, 2024.

Varliero, S., Jamali Alamooti, S., Campo, F. P., Cappello, G., Cappello, S., Caserini, S., Comazzi, F., Macchi, P., and Raos, G.: Assessing the Limit of CO2 Storage in Seawater as Bicarbonate-Enriched Solutions, Molecules, 29, 4069, https://doi.org/10.3390/molecules29174069, 2024a.

Varliero, S., Buono, A., Caserini, S., Raos, G., and Macchi, P.: Chemical Aspect of Ocean Liming for CO2 Removal: Dissolution Kinetics of Calcium Hydroxide in Seawater, ACS Eng. Au, 4, 422–431, https://doi.org/10.1021/acsengineeringau.4c00008, 2024b.

Varliero, S., Buono, A., Caserini, S., Raos, G., and Macchi, P.: Chemical Aspect of Ocean Liming for CO2 Removal: Dissolution Kinetics of Calcium Hydroxide in Seawater, ACS Eng. Au, 4, 422–431, https://doi.org/10.1021/acsengineeringau.4c00008, 2024b.

Wang, H., Pilcher, D. J., Kearney, K. A., Cross, J. N., Shugart, O. M., Eisaman, M. D., and Carter, B. R.: Simulated Impact of Ocean Alkalinity Enhancement on Atmospheric CO2 Removal in the Bering Sea, Earth's Future, 11, e2022EF002816, https://doi.org/10.1029/2022EF002816, 2023.

Weibull, W.: A Statistical Distribution Function of Wide Applicability, Journal of Applied Mechanics, 1951.

Xin, X., Goldenberg, S. U., Taucher, J., Stuhr, A., Arístegui, J., and Riebesell, U.: Resilience of Phytoplankton and Microzooplankton Communities under Ocean Alkalinity Enhancement in the Oligotrophic Ocean, Environ. Sci. Technol., 58, 20918–20930, https://doi.org/10.1021/acs.est.4c09838, 2024.

Yang, B., Leonard, J., and Langdon, C.: Seawater alkalinity enhancement with magnesium hydroxide and its implication for carbon dioxide removal, Marine Chemistry, 253, 104251, https://doi.org/10.1016/j.marchem.2023.104251, 2023.